Fabrication process of a coaxial plasmonic metamaterial

Marie Anne van de Haar and Albert Polman*
Center for Nanophotonics, FOM Institute AMOLF, Science Park 104, 1098 XG, Amsterdam, the Netherlands
*polman@amolf.nl

Abstract: We report, in full detail, the experimental fabrication process of a coaxial plasmonic metamaterial which is designed to operate in the UV/visible part of the spectrum. The metamaterial consists of ultra-thin wall (13–15 nm) dielectric (Si or HSQ) coaxial cylinders with a well defined diameter (>100 nm) embedded in silver or gold. We demonstrate the fabrication process on both a SiO_2 and Si substrate, where fabrication on a 1 μm thick Si membrane results in nearly freestanding structures. The process starts with creating an HSQ etch mask, using electron beam lithography. The structures are then transferred into the substrate with reactive ion etching, followed by metal infilling using a newly developed physical vapor deposition technique. Finally, the metamaterial surface is polished and made optically accessible with focused ion beam milling under grazing angles.

OCIS codes: (160.1245) Artificially engineered materials; (160.3918) Metamaterials; (160.4670) Optical materials; (220.3740) Lithography; (220.4241) Nanostructure fabrication; (230.7400) Waveguides, slab.

References and links

1. V. G. Veselago, "The electrodynamics of substances with simultaneously negative values of ε and μ," Phys. Usp. **10**, 509 (1968).
2. E. Verhagen, R. de Waele, L. Kuipers, and A. Polman, "Three-dimensional negative index of refraction at optical frequencies by coupling plasmonic waveguides," Phys. Rev. Lett. **105**, 223901 (2010).
3. R. Maas, J. Parsons, N. Engheta, and A. Polman, "Experimental realization of an epsilon-near-zero metamaterial at visible wavelengths," Nature Photon. **7**, 907–912 (2013).
4. R. A. Shelby, D. R. Smith, and S. Schultz, "Experimental verification of a negative index of refraction," Science **292**, 77–79 (2001).
5. J. Valentine, S. Zhang, T. Zentgraf, E. Ulin-Avila, D. A. Genov, G. Bartal, and X. Zhang, "Three-dimensional optical metamaterial with a negative refractive index," Nature **455**, 376–379 (2008).
6. G. Dolling, M. Wegener, C. M. Soukoulis, and S. Linden, "Negative-index metamaterial at 780 nm wavelength," Opt. Lett. **32**, 53–55 (2007).
7. C. Rockstuhl, T. Zentgraf, H. Guo, N. Liu, C. Etrich, I. Loa, K. Syassen, J. Kuhl, F. Lederer, and H. Giessen, "Resonances of split-ring resonator metamaterials in the near infrared," Appl. Phys. B **84**, 219–227 (2006).
8. C. M. Soukoulis, S. Linden, and M. Wegener, "Negative refractive index at optical wavelengths," Science **315**, 47–49 (2007).
9. J. A. Dionne, E. Verhagen, A. Polman, and H. A. Atwater, "Are negative index materials achievable with surface plasmon waveguides? a case study of three plasmonic geometries," Opt. Express **16**, 19001–19017 (2008).
10. R. de Waele, S. P. Burgos, H. A. Atwater, and A. Polman, "Negative refractive index in coaxial plasmon waveguides," Opt. Express **18**, 12770–12778 (2010).
11. S. P. Burgos, R. de Waele, A. Polman, and H. A. Atwater, "A single-layer wide-angle negative-index metamaterial at visible frequencies," Nat. Mater. **9**, 407–412 (2010).
12. M. A. van de Haar, R. Maas, H. Schokker, and A. Polman, "Experimental Realization of a Polarization-Independent Ultraviolet/Visible Coaxial Plasmonic Metamaterial," Nano Lett. **14**, 6356–6360 (2014).

#254759 Received 1 Dec 2015; revised 8 Feb 2016; accepted 8 Feb 2016; published 23 Feb 2016

13. M. Peuker, M. H. Lim, H. I. Smith, R. Morton, A. K. van Langen-Suurling, J. Romijn, E. W. J. M. van der Drift, and F. C. M. J. M. van Delft, "Hydrogen silsesquioxane, a high-resolution negative tone e-beam resist, investigated for its applicability in photon-based lithographies," Microelectron. Eng. **61-62**, 803–809 (2002).
14. N. Yahya, *Carbon and Oxide Nanostructures: Synthesis, Characterisation and Applications* (Springer, 2010).
15. A. E. Grigorescu and C. W. Hagen, "Resists for sub-20-nm electron beam lithography with a focus on hsq: state of the art," Nanotechnology **20**, 292001 (2009).
16. C. L. Frye and W. T. Collins, "Oligomeric silsesquioxanes, (hsio3/2)n," J. Am. Chem. Soc. **92**, 5586–5588 (1970).
17. S. Choi, N. Jin, V. Kumar, I. Adesida, and M. Shannon, "Effects of developer temperature on electron-beam-exposed hydrogen silsesquioxane resist for ultradense silicon nanowire fabrication," J. Vac. Sci. Technol. B **25**, 2085–2088 (2007).
18. F. C. M. J. M. van Delft, "Delay-time and aging effects on contrast and sensitivity of hydrogen silsesquioxane," J. Vac. Sci. Technol. B **20**, 2932–2936 (2002).
19. Y. Chen, H. Yang, and Z. Cui, "Effects of developing conditions on the contrast and sensitivity of hydrogen silsesquioxane," Microelectron. Eng. **83**, 1119–1123 (2006).
20. F. Fruleux-Cornu, J. Penaud, E. Dubois, M. François, and M. Muller, "An optimal high contrast e-beam lithography process for the patterning of dense fin networks," Mater. Sci. Eng. C **26**, 893–897 (2006).
21. Y. Georgiev, W. Henschel, A. Fuchs, and H. Kurz, "Surface roughness of hydrogen silsesquioxane as a negative tone electron beam resist," Vacuum **77**, 117–123 (2005).
22. N. Clark, A. Vanderslice, R. Grove, and R. R. Krchnavek, "Time-dependent exposure dose of hydrogen silsesquioxane when used as a negative electron-beam resist," J. Vac. Sci. Technol. B **24**, 3073–3076 (2006).
23. H. F. Winters and J. W. Coburn, "Surface science aspects of etching reactions," Surf. Sci. Rep. **14**, 162–269 (1992).
24. Z. Cui, *Nanofabrication: Principles, Capabilities, and Limits* (Springer Science, 2008).
25. R. Legtenberg, H. Jansen, M. de Boer, and M. Elwenspoek, "Anisotropic reactive ion etching of silicon using sf_6 / o_2 / chf_3 gas mixtures," J. Electrochem. Soc. **142**, 2020–2028 (1995).
26. S. Grigoropoulos, E. Gogolides, A. D. Tserepi, and A. G. Nassiopoulos, "Highly anisotropic silicon reactive ion etching for nanofabrication using mixtures of sf_6/chf_3 gases," J. Vac. Sci. Technol. B **15**, 640–645 (1997).
27. E. Gogolides, S. Grigoropoulos, and A. G. Nassiopoulos, "Highly anisotropic room-temperature sub-half-micron si reactive ion etching using fluorine only containing gases," Microelectron. Eng. **27**, 449–452 (1995).
28. V. Gianneta, A. Olziersky, and A. Nassiopoulou, "Si nanopatterning by reactive ion etching through an on-chip self-assembled porous anodic alumina mask," Nanoscale Res. Lett. **8**, 71 (2013).
29. H. Jansen, H. Gardeniers, M. d. Boer, M. Elwenspoek, and J. Fluitman, "A survey on the reactive ion etching of silicon in microtechnology," J. Micromech. Microeng. **6**, 14 (1996).
30. R. d´Agostino and D. L. Flamm, "Plasma etching of si and sio_2 in sf_6–o_2 mixtures," J. Appl. Phys. **52**, 162–167 (1981).
31. V. M. Donnelly and A. Kornblit, "Plasma etching: Yesterday, today, and tomorrow," J. Vac. Sci. Technol. A **31**, 050825 (2013).
32. D. L. Olynick, J. A. Liddle, and I. W. Rangelow, "Profile evolution of cr masked features undergoing hbr-inductively coupled plasma etching for use in 25 nm silicon nanoimprint templates," J. Vac. Sci. Technol. B **23**, 2073–2077 (2005).
33. Walker, Z. H., Ogryzlo, and E. A., *Rate constants for the etching of intrinsic and doped polycrystalline silicon by bromine atoms*, vol. 69 (American Institute of Physics, Melville, NY, ETATS-UNIS, 1991).
34. D. L. Olynick, J. A. Liddle, B. D. Harteneck, S. Cabrini, and I. W. Rangelow, "Nanoscale pattern transfer for templates, nems, and nano-optics," vol. 6462, pp. 64620J–64620J–8. 10.1117/12.705033.
35. S. Bouchoule, G. Patriarche, S. Guilet, L. Gatilova, L. Largeau, and P. Chabert, "Sidewall passivation assisted by a silicon coverplate during cl_2–h_2 and hbr inductively coupled plasma etching of inp for photonic devices," J. Vac. Sci. Technol. B **26**, 666–674 (2008).

1. Introduction

Optical metamaterials are artificial materials composed of sub-wavelength building blocks which can be engineered to have optical properties which are not found in nature, such as a negative index of refraction [1, 2] or an index near zero [3]. An important class of optical metamaterials is composed of sub-wavelength metal resonant structures with a magneto-electric response (e.g. split ring resonators), embedded in a dielectric material. These resonance based metamaterials have been demonstrated experimentally in the infra-red and longer wavelength regime [4, 5, 6]. However, realizing these antenna-based metamaterials for shorter wavelengths has proven to be very difficult because the resonator size scales with the operating wavelength [7]. These fabrication difficulties, together with the narrow bandwidth and relatively

#254759 Received 1 Dec 2015; revised 8 Feb 2016; accepted 8 Feb 2016; published 23 Feb 2016

high losses at the resonance frequency [8] can be circumvented by using plasmonic metamaterials. This class of metamaterials does not rely on localized resonances, but are built up from alternating metal/dielectric layers that support surface plasmon polaritons (SPPs) [9]. Properly designing the SPP coupling traveling on the metal/dielectric interfaces by tuning the dimensions of these metal/dielectric stacks can, as in case for the resonance-based metamaterials, also result in special optical properties as negative and near-zero refractive index [2, 3]. However, these planar geometries only work for TM polarized light and are thus highly polarization dependent.

A similar, polarization independent, geometry was first proposed in 2010 [10, 11], consisting of sub-wavelength semiconductor rings embedded in metal. As for the planar geometries, the optical properties are the result of the coupling of SPPs traveling on each metal/dielectric interface. In order to get sufficient coupling it is crucial to have very small channel widths, in the order of 10-30 nm, which was the main challenge of the described fabrication process. This coupling, and thus the optical properties, can be tuned by changing the material and cylinder geometries. Using Si rings with a wall-thickness of 15–30 nm and an outer diameter in the order of 100–180 nm, this material has been shown to exhibit a near-zero and negative refractive index in the visible part of the spectrum [12].

Here, we present the fabrication process of a polarization independent metamaterial, consisting of hollow Si or hydrogen silsesquioxane (HSQ) cylinders embedded in metal.We show the successful fabrication process of Si coaxes on a Si chip, almost freestanding structures on 1 μm thick membranes as well as the fabrication of HSQ coaxes, which has a refractive index very similar to glass [13], on a SiO_2 substrate. The silicon structures were infilled with Ag, the HSQ on glass samples both with Ag and Au.

Figure 1 shows a sketch of the total fabrication process. We start with electron beam lithography (EBL) using the negative high-resolution resist HSQ. The HSQ patterns can be used as etch mask to transfer the structures into the substrate using reactive ion etching (RIE). Next, we infill the structures with metal using a newly developed electron beam physical vapor deposition (EBPVD) method followed by a polishing step with a focused ion beam (FIB) to smoothen the surface and make the coaxes optically accessible. Each of these steps will be explained in detail in the next sections of this paper.

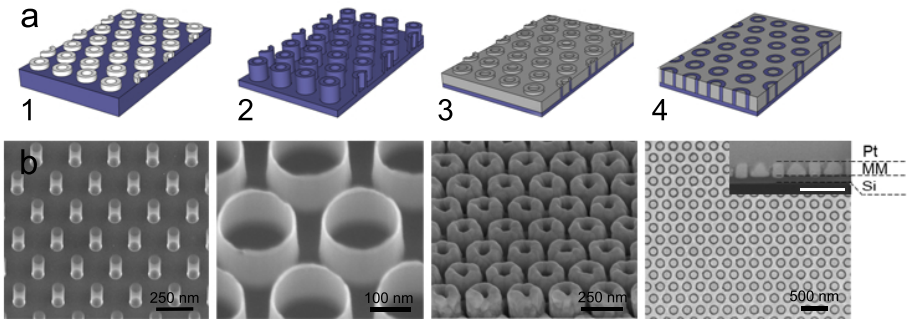

Fig. 1. Fabrication process of the coaxial metamaterial. (a) Sketch and (b) SEM images of the individual steps: 1. EBL on Si, Si membrane or SiO_2 substrate, 2. RIE etching to transfer the structures into the substrate, 3. Metal deposition using a newly developed EBPVD method, and 4. Polishing the surface with the FIB under grazing incidence.

#254759 Received 1 Dec 2015; revised 8 Feb 2016; accepted 8 Feb 2016; published 23 Feb 2016

1.1. Resolution in electron beam lithography

In order to obtain feature sizes as small as 10 nm, we need a very high resolution in the EBL process. The resolution of the EBL process is determined by the properties of the used resist, the lithographic system and processing conditions. An important aspect which limits the resolution is the scattering of electrons in the resist itself and the substrate underneath the resist. There are two types of elastic scattering: forward and back-scattering. Forward scattering is the small-angle deflection of electrons that enter the resist. This leads to an overall increase of the beam diameter, resulting in the exposure of a larger area in the resist. This effect can be reduced by using thinner resist films, a resist with small atomic weights, or increasing the beam energy. In back-scattering the electrons are deflected at large angles, where areas far from the incoming beam can be exposed. This effect occurs mostly in the substrate. This phenomenon is also known as the proximity effect, which is especially a problem for dense arrays where certain areas of a resist receive a larger dose than intended due to backscattered electrons from neighboring areas. Back-scattering can be reduced by using a very thin substrate or a substrate with a low atomic weight, or using electrons with lower energy.

Since the majority of the resist is transformed by secondary electrons rather than the direct electron beam, it is important to consider these electrons as well in order to determine the optimal resolution of the EBL process. Secondary electrons originate from inelastic collisions with the electrons in the molecules of the resist or substrate and lead to an effective widening of the beam diameter. Secondary electrons do not contribute to the proximity effect since their range in the resist is only a few nanometers.

Interestingly, both increasing and decreasing the electron voltage can result in a higher resolution. As the electron energy is increased, less forward scattering results in more vertical wall profiles and thus better resolution. However, higher electron energy also results in more back-scattering which increases the proximity effect. For thin or low atomic weight resists and substrates, a high electron energy ($>$20 keV) will generally lead to the highest resolution. Using low energy electrons ($<$5 keV) can also result in higher resolution since the generation rate of back-scattered electrons is decreased [14]. Here, we use a 30 or 100 keV electron beam, where 100 keV results in the highest resolution EBL process.

High resolution resists typically have a small molecule size, small atomic weight and require a relatively high exposure dose (low sensitivity). The smaller size of the molecules allows cross-linking or chain scission to happen at a smaller scale, while the low atomic weight reduces the electron scattering in the resist. The lower sensitivity typically leads to less proximity effects, which increases the resolution especially for dense arrays. However, a lower sensitivity requires a larger exposure dose, which results in a more time consuming process.

The sensitivity of the resist depends on several factors. In general, a larger molecule requires a smaller exposure dose since it has a larger cross section and hence a higher probability of electron interaction. The sensitivity is also affected by the electron energy, where the sensitivity is increased for lower energy electrons (as long as the electron energy is still large enough such that the electrons can travel to the bottom of the resist layer). This is due to an increased probability of the electrons to interact with the resist rather than the underlying substrate. On the other hand, using a low atomic weight or thin membrane substrate results in a higher required dose due to the decreased generation rate of back-scattered electrons.

The inorganic negative high resolution resist hydrogen silsesquioxane (HSQ), meets the requirement of consisting of relatively small molecules. It requires a relatively high exposure dose compared to most (organic) resists and has a high etch resistance which is needed to transfer the patterns into the Si substrate [15]. A disadvantage of HSQ is its low contrast, which can be changed by adjusting the development and baking procedure [17, 18, 15, 19, 20, 21]. This tunability is convenient, but it also reflects the extreme sensitivity of HSQ to environmental

#254759 Received 1 Dec 2015; revised 8 Feb 2016; accepted 8 Feb 2016; published 23 Feb 2016

changes and pollution. A change of just 1 °C in the developing temperature leads to a variation of 11% in contrast, 5% in the saturation and 49% in the on-set dose [19]. Exposure to air for only 1 hour can increase the feature size by 66% [22].

1.2. Reactive ion etching

For the fabrication of coaxial Si cylinders, the HSQ pattern is transferred into the substrate using RIE. RIE is a dry-etching technique which is based on two principles: plasma, or radical, etching and physical sputtering of the substrate with ions provided by the plasma. The first is characterized by minimal ion bombardment and purely chemical etching, leading to very selective and fast, but isotropic etches. This process is usually dominant for very low bias and high gas pressure. However, for many substrate materials there is no chemical etchant available. In these cases the sample can be etched using sputtering with a directed ion flow. The latter technique is usually very slow (1–30 nm/min), but can also be very anisotropic and is in principle applicable to any substrate. By combining both techniques by adding a few well-chosen reactive chemicals to the etch mixture while using a relatively large bias and/or low density, the etch rate, selectivity and isotropy of the etch can be controlled.

Although there are some general guidelines for the etching behavior, it is important to keep in mind that the interplay between chemical etching and physical sputtering of the substrate is very complex and not straightforward. To mention an example, the etch rate of Si exposed to both XeF_2 and Ar^+ ions is much greater than the sum of the etch rates for exposure to the Ar_2 and XeF_2 separately [23]. The reason is that the reactive XeF_2 does not only enhance the etch rate by reacting with the substrate to form volatile molecules, but adding Ar^+ ions also modifies the surface reactions in such a way that radicals can react stronger with the substrate. Adding reactive chemicals to the etching mixture can not only enhance the etch rate but can also inhibit the etching by forming a passivation layer with a high etch resistance. This technique is often used in etch mixtures containing both ions and reactive chemicals to make the etch more directional. Sidewalls that are not exposed to the ions are then covered by the resistive layer, while normal to the ion path this layer will be removed by ion bombardment.

Clearly, in order to develop an etch recipe we have several parameters to optimize, which have a complex interplay with each other [24, 25]. It is not straightforward to predict a priori which chemicals should be used in which (relative) concentrations and how changing the chemicals influences the etch rate, anisotropy and selectivity. However there are some general guidelines that can be used when developing an etch recipe. Increasing the radio frequency (RF) power generally leads to more sputtering and a higher etch rate, while increasing the inductively coupled plasma (ICP) power generally leads to more lateral etching and thus less anisotropy. Lastly, increasing the temperature promotes chemical reactions, but can also increase lateral etching because surface radicals become more mobile. Using cryogenic temperatures can enhance the forming of a passivation layer because the low temperature prevents compounds from escaping the surface.

For our fabrication process there are two main criteria which determine the succes of the etch recipe: selectivity and anisotropy. Due to the very thin side walls, our structures are very sensitive to slightly isotropic etching which results in holes in the side walls and collapsing of the rings. Therefore we cannot compromise on the anisotropy of the etch, which for most etch recipes results in a limited maximum height of the Si coaxes. To fabricate larger aspect ratios while maintaining the anisotropy, one could either use a thicker HSQ mask or switch to different etching chemicals. However, increasing the resist thickness will decrease the resolution of the EBL process, resulting in thicker side walls (Section 1.1).

Here, we develop two anisotropic etch recipes which successfully transfer HSQ cylinders into the Si substrate. The first is based on CHF_3 and SF_6, the second on HBr. For both etch recipes

#254759 Received 1 Dec 2015; revised 8 Feb 2016; accepted 8 Feb 2016; published 23 Feb 2016

we use a low pressure recipe and relatively high ion energies, such that the lateral movement of the ions is minimized.

2. Electron beam lithography using HSQ

2.1. Method

The first step in the many-step fabrication process is patterning the substrates with hollow cylinders of the negative high resolution resist HSQ. The metamaterial was fabricated on three different kinds of substrates: SiO_2 slides (1 mm thick borosilicate glass slides from Menzel), 500–550 μm thick Si(100) chips (WRS Materials) and 1 μm thick 1.3×1.3 μm^2 Si(100) membranes supported by a 300 μm thick 10×10 mm^2 Si frame (Norcada). Before the fabrication is started, the samples are first base-piranha cleaned (5:1:1 solution of dH_2O:NH_2OH:H_2O_2) at 75 °C for about 20 minutes. The samples are rinsed in demi-water and blow-dried with N_2. The silicon membranes were used fresh from the packaging without any cleaning. Before spin coating, all substrates were baked for 5 minutes at 200 °C to completely dry the surface. To be able to spin coat the membranes, we stuck them on top of a Si chip using copper tape or a thin layer of acetone dissoluble glue. After baking, the samples are cooled to room temperature with a N_2-flow for about 10 s. Then the samples were immediately spin coated with, depending on the desired resist thickness, (dilutions of) HSQ Fox-12, FOx-14 or FOx-15 (Dow Corning) for 45 seconds at 2000 rpm, with a closed lid. If thin resist layers were desired, the standard HSQ solutions were diluted with MIBK. To obtain a higher resolution the samples were baked at 90 °C for 45 minutes, instead of the typical two-step baking procedure of 120 s at 150 °C followed by 120 s at 220 °C [20]. Baking at lower temperatures increases the resolution, but decreases the sensitivity, meaning that a higher dose is needed when exposing the HSQ to the electron beam [21]. In case of the SiO_2 substrates the samples were made conductive by spin coating a thin layer of an aqueous solution with a conducting polymer (Espacer 300Z, Showa Denko) for 45 s at 3000 rpm with a closed lit. After spin coating the samples were dried at room temperature for 2 minutes before a 5 minutes bake at 180 °C. The HSQ layer thickness was measured by scratching the sample and using a height profilometer. The resist thickness was typically 200 nm (using undiluted HSQ FOX-14 or FOX-15), but could be varied between 50–500 nm depending on the HSQ concentration and age, type and treatment of substrate and spinning conditions.

Depending on the desired resolution, either a 30 keV beam, using a Raith e-LINE EBL system, or a 100 keV from a Vistec EBPG5000Plus HR 100 system with a small aperture was used to write rings into the HSQ. Because the sensitivity of HSQ is very dependent on the exact spinning, storing and baking conditions (e.g. thickness of the resist, baking temperature and time [21], substrate, writing voltage, age of the HSQ, time between spin coating and baking, time between baking and writing [18]) the optimum exposure dose varies between different samples. Typically, for a resist thickness of 200 nm and a 1 μm thick Si membrane substrate, we used $\sim$300 $\mu C/cm^2$ for 30 keV EBL, and $\sim$14000 $\mu C/cm^2$ for the 100 keV e-beam writing. In general, membrane samples require a higher dose compared to thicker substrates, due to the reduced amount of back-scattered electrons in case of thinner substrates. Also, thicker resist layers require a higher dose. Longer waiting times between spin coating and exposure or exposure and developing will both lead to lower writing doses (higher sensitivity) but slightly lower resolution due to partly cross-linking of HSQ over time [18].

After writing, the structures are developed in tetramethylammonium hydroxide (TMAH) for 1 minute at 50 °C, rinsed in dH_2O for 30 s and dipped into isopropanol (IPA). The samples were dried in a critical point dryer to prevent collapsing or displacement of the structures. For the non-membrane samples we used a 25% TMAH solution, for the membranes we diluted this to a 5% solution to improve the adhesion of the structures onto the substrate, however,

#254759 Received 1 Dec 2015; revised 8 Feb 2016; accepted 8 Feb 2016; published 23 Feb 2016

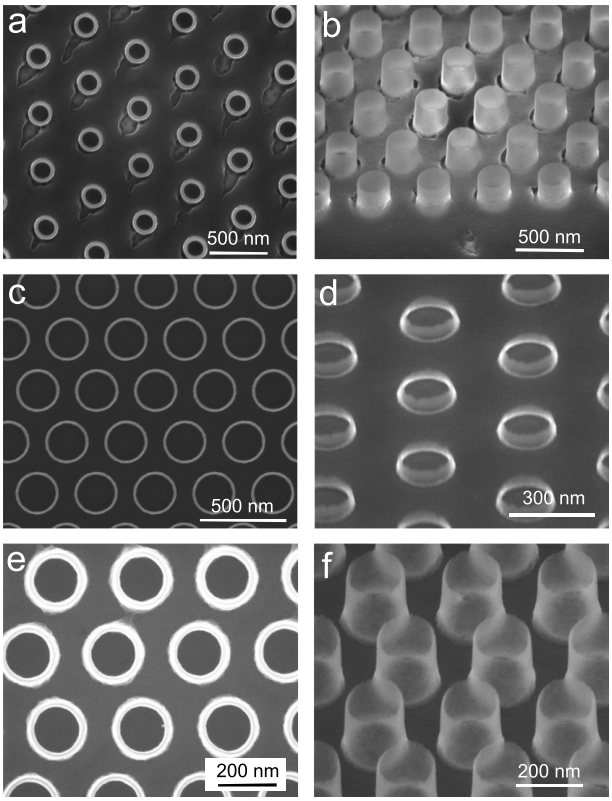

Fig. 2. HSQ coaxes after exposure to a 30 keV electron beam and development in a 25% TMAH solution in water on a (a,b) SiO_2 and (c-f) Si substrate. (a,c,e) show a top view, whereas (b,d,f) show a tilted view. The structures in (c,d) are ∼80nm in height, the structures in (b,f) are ∼200 nm tall. SEM images are taken using a 5 keV electron beam.

this results in a slightly lower resolution. Developing at 50 °C instead of room temperature increases the resolution and decreases the feature roughness [19, 20]. In Fig. 2 we show SEM images of developed HSQ coaxes on different substrates, where (a,b) show structures on a SiO_2 substrate and (c-f) shows the successful fabrication on a Si substrate. As shown in Fig. 3, the described process results in very conformal fabrication of larger areas (typically 20×20 μm^2 fields were written, but in principle the field size is limited by the write field area for which no stage movement is needed, which is typically a few mm). In Figs. 2.4(e) and 2.4(f) we show that it is possible to fabricate very high aspect ratio coaxes having a height of over 400 nm, with a diameter of 80 nm and a wall thickness of about 20 nm.

2.2. *Critical point dryer*

As described in Section 2.1, all samples were dried in a critical point dryer after development. Figure 5 shows a patterned sample after development that was dried in air instead, i.e. without critical point dryer. In this case, coaxes with relatively low aspect ratio (having a height of typically $<$150 nm for $>$100 nm diameter rings) are displaced over the sample surface (Figs. 5(a) and 5(b), whereas longer coaxes (with a height of typically $>$150 nm for $<$300 nm diameter rings) collapse and cluster together by the pressure of the liquid droplet. The interfacial tension between the liquid/air interface of the drying solvent droplet can be prevented by using a crit-

#254759 Received 1 Dec 2015; revised 8 Feb 2016; accepted 8 Feb 2016; published 23 Feb 2016

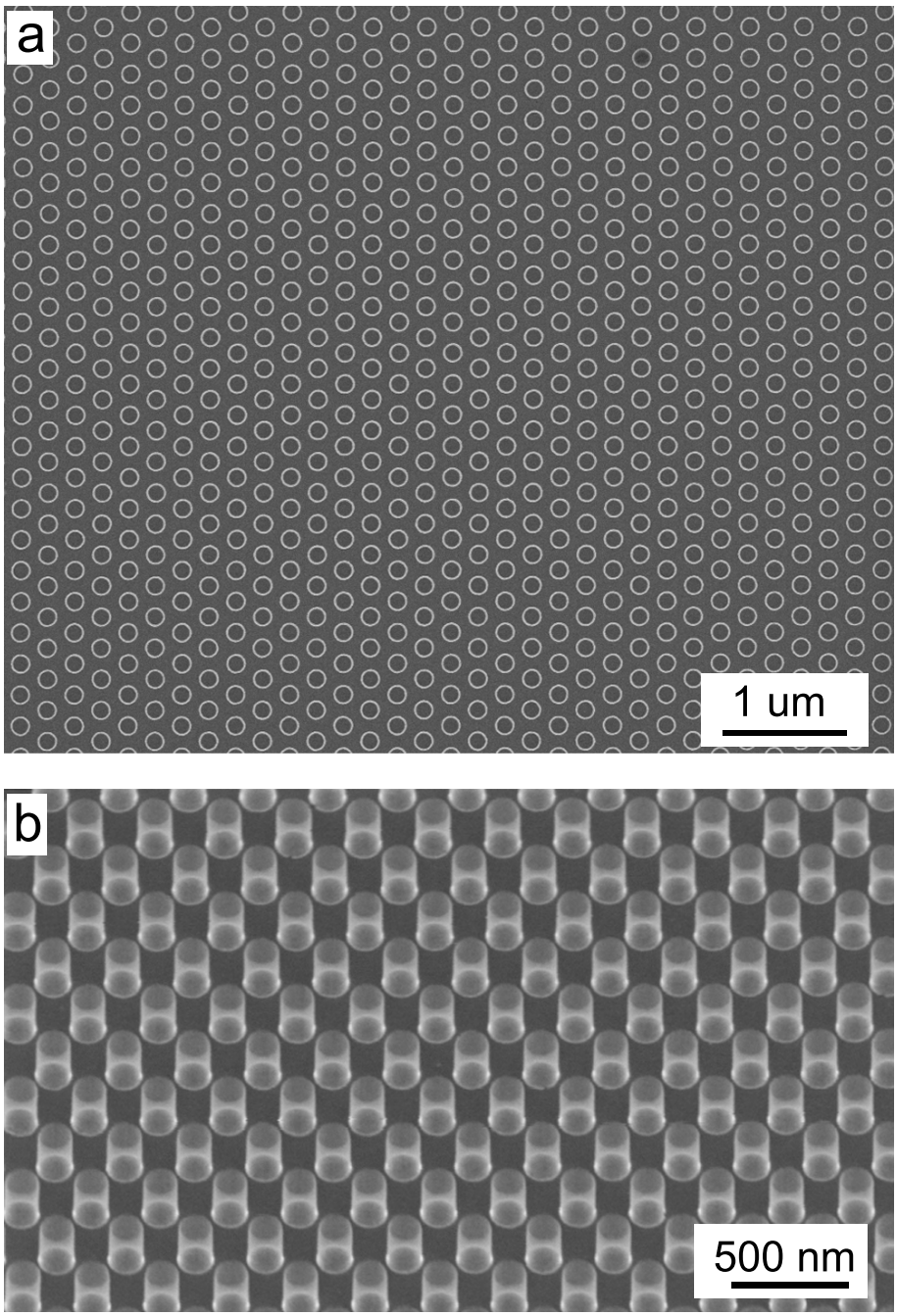

Fig. 3. (a) Top and (b) tilted view of a hexagonal array of HSQ coaxes, having an outer diameter of 150 nm, a wall thickness of 5–10 nm and a height of 220 nm on a 1 μm thick Si membrane after exposure of a 100 keV electron beam and development in a 5% TMAH solution in water. SEM images are taken using a 5 keV electron beam.

#254759 Received 1 Dec 2015; revised 8 Feb 2016; accepted 8 Feb 2016; published 23 Feb 2016

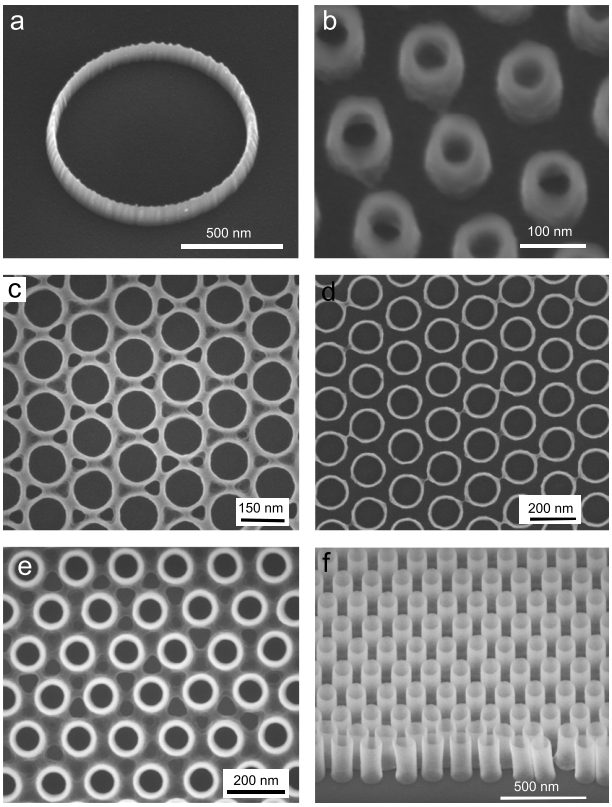

Fig. 4. Limitations in resolution of EBL with HSQ. (a) There are basically no limits on the maximum diameter. This ring is 1 μm in diameter. (b) The minimum ring diameter is about 85 nm for 100 nm tall rings. Decreasing the radius further results in completely filled rings. (c) If the ring-to-ring distance is smaller than $\sim$30 nm the coaxes start to merge. The ring-to-ring distance was designed here to be 20 nm. In (d) the ring-to-ring distance is 30 nm. (e,f) Top and tilted view of 410 nm tall coaxes on a Si membrane (100 keV). The ring diameter is 130 nm and the wall thickness is about 16 nm. SEM images are taken using a 5 keV electron beam.

#254759 Received 1 Dec 2015; revised 8 Feb 2016; accepted 8 Feb 2016; published 23 Feb 2016

ical point dryer which replaces the solvent (usually isopropanol) with liquid CO_2, after which the pressure and temperature inside the sample chamber is increased to go to the critical point of CO_2. Then, the CO_2 is vented out of the chamber, resulting in drying the sample without any liquid/air interface. For this reason, all samples described in this thesis are dried after development using a critical point dryer. However, a critical point dryer is not necessary after the HF dip later on in the fabrication process. The reason is that the adhesion of the rings is much stronger during this drying process because the rings are etched into the Si before the HF dip, resulting in more rigid structures which are stably attached to the surface.

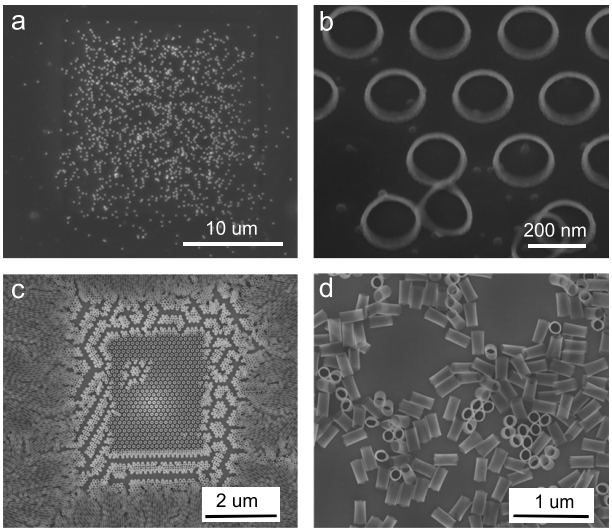

Fig. 5. Examples of HSQ coaxes where the samples are dried in air after development instead of using the critical point dryer. Short coaxes (a,b) (typically $<$150 nm) are displaced over the sample, whereas long coaxes (c,d) (typically $>$150 nm) collapse and cluster together by the surface pressure of the drying liquid droplet. The HSQ coaxes in this figure are 80 nm (a,b) and 335 nm (c,d) nm in height. All SEM images are taken using a 5 keV electron beam.

2.3. HSQ adhesion on Si membranes

For both the silicon and SiO_2 substrates the samples were developed in a 25% TMAH solution in water at 50 °C. As can been seen in Fig. 2, this results in structures with extremely thin side walls ($<$10 nm), with good adhesion on both Si and SiO_2. Clearly, the minimum feature size is increased if the resist thickness is increased.

However, developing the Si membrane samples with this high concentration of TMAH causes adhesion problems, as shown in Figs. 6(a) and 6(b). Due to bad adhesion of the HSQ after development, the individual rings are washed away and the over-exposed fields, where the individual rings are all merged together due to proximity effects, are displaced over the substrate after development. The over-exposed fields release from the substrate during imaging with a 5 keV beam, demonstrating the bad adhesion.

Clearly, a 25% TMAH solution is too aggressive on Si membranes. Several surface treatments, such as charging the surface with an RIE oxygen descum or thermal annealing before applying the HSQ did not improve the adhesion sufficiently. Figures 6(d) and 6(e) shows the effect of spincoating HDMS primer underneath the HSQ for 1 min. at 4000 rpm and baking

#254759 Received 1 Dec 2015; revised 8 Feb 2016; accepted 8 Feb 2016; published 23 Feb 2016

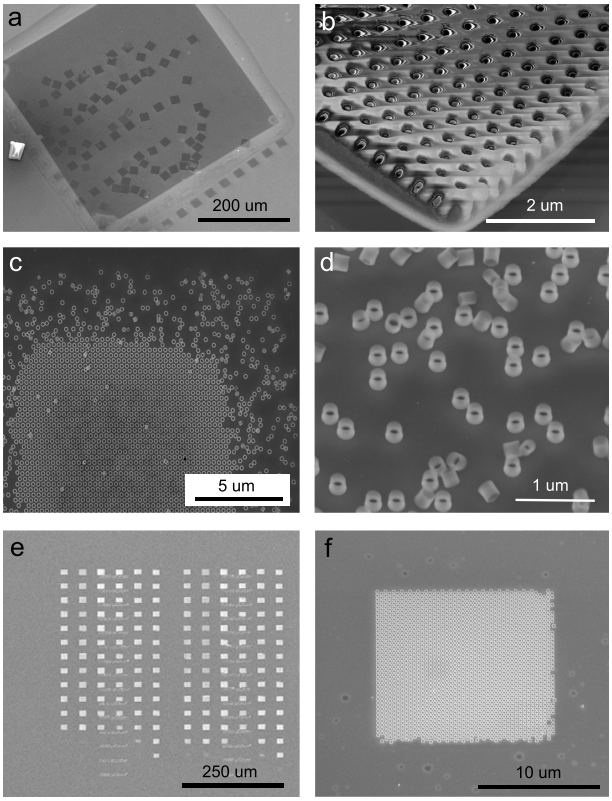

Fig. 6. Adhesion problems of HSQ on Si membranes. (a-d) Development with 25% and (e,f) 5% TMAH solution in water at 50 °C. The darker area in (a) is a 500×500 μm Si membrane, surrounded by thick Si (lighter grey) to support the membrane. The smaller squares are 20×20 μm fields of exposed and developed HSQ. A zoom of one of these fields is shown in (b), where the bottom left corner is lifted from the substrate under influence of the electron beam during imaging with the SEM. In the experiments shown in (c,d) a HDMS primer was spincoated underneath the HSQ, where (c) shows an 20×20 μm field of exposed and developed HSQ rings, and (d) is a zoom where the individual rings can be seen. The squares in (e) are fields of exposed and developed HSQ rings developed using a 5% TMAH solution. In these fields the dose is increasing from top to bottom, while from left to right different geometries are written. A close up of a hexagonal array of coaxes is shown in (f). SEM images are taken using a 5 keV electron beam.

#254759 Received 1 Dec 2015; revised 8 Feb 2016; accepted 8 Feb 2016; published 23 Feb 2016

at 180 °C before applying the HSQ. Although it does improve the adhesion somewhat, the rings are still displaced over the substrate. The adhesion problems can be solved by using a 5% TMAH solution instead of the 25%. The result is shown in Figs. 6(e) and 6(f). The resolution is slightly decreased by developing with lower concentrations, but this can be compensated by using 100 keV EBL instead of 30 keV. Figure 3 shows the result of HSQ coaxes on top of a 1 μm thick membrane after exposure with a 100 keV electron beam and development in 5% TMAH solution in water at 50°C. Using 100 keV EBL on 200–250 nm thick HSQ on a Si membrane results in a wall thickness as small as 10–15 nm is achieved. This resolution is similar to the results we obtained in Figs. 2(b) and 2(c), where a 30 keV beam was used to write structures in a 50–80 nm thick HSQ layer on a thick Si substrate.

2.4. Limits of EBL using HSQ

The optimized procedure as discussed in Section 2.3, using 100 keV EBL, leads to HSQ rings with a wall thickness of 10 nm and a height up to 250 nm on a Si membrane. Figure 2.4 summarizes some other limiting factors that we found in writing HSQ rings on Si, Si membranes and SiO_2 substrates using thick HSQ layers of 200–250 nm.

Basically, there are no limits on the maximum ring diameter as long as they fit within one write field of the EBL system which is 2 mm for the Raith system used to write the 20 and 30 keV samples. We have successfully fabricated rings with a 1 μm diameter (Fig. 2.4(a)). The minimum outer ring diameter is defined by proximity effects and the sensitivity and resolution of the resist, the first being determined by the voltage of the electron beam, the latter by the aging and handling of the HSQ before writing (see Section 1). We found a minimum outer diameter of 100 nm (see Fig. 2.4(b)). Decreasing the diameter further results in solid rings where the gap in the center is completely filled.

Limitations in the closest ring-to-ring distance are also determined by proximity effects and sensitivity and resolution of the resist. We successfully fabricated a ring-to-ring distance of about 30 nm (Fig. 2.4(c)). Decreasing this distance further results in bridges between the rings at their closest spacing position. (Fig. 2.4(d)).

The maximum height of the coaxes is not well defined, but a trade off between resolution and height. We fabricated 410 nm tall HSQ coaxes with a wall thickness of about 16 nm.

3. Reactive ion etching

3.1. Reactive ion etching of Si using SF_6 and CHF_3

For the next step in the fabrication process of Si coaxes, the HSQ structures are used as etch mask to etch the Si substrate with a very anisotropic reactive ion etch. In this section we discuss the RIE etching of Si using SF_6 and CHF_3, which is a well known mixture to anisoptropically etch Si [26, 27, 28]. Both chemicals form radicals in the plasma (F^*, SF_5^* and CF_2^*) which can etch Si by forming the volatile products SiF_4, HF and SiF_4, or form the etching inhibitors $Si_xS_yF_z$ (only if cryogenic cooling is used) and $Si_xC_yF_6$, which protect the side walls of the structures during the etching process [29]. At room temperature SF_6 is used as etchant, whereas CHF_3 mainly acts as inhibitor to enhance the anisotropy by forming a polymer layer on the surfaces. The ion bombardment need to be optimized such, that it is efficient enough to be able to break through the protective layer on the substrate without damaging the polymer on the side walls of the structures. The relative efficiencies of the chemical etching, protecting and ion bombardment processes can be tuned by changing the plasma conditions, as explained in Section 1.2.

Small amounts of O_2 ($<5\%$) in the plasma are known to increase the etch rate by reacting with CF_x^* radicals to form CO_2 and COF_2, which increases the reactive F-ion concentration [30]. We found that for our recipe the addition of O_2 also increases the Si:HSQ selectivity,

#254759 Received 1 Dec 2015; revised 8 Feb 2016; accepted 8 Feb 2016; published 23 Feb 2016

which increases the maximum height of the Si structures that can be achieved. However, due to consumption of the CF_x^*, the formation of the protective polymer layer is suppressed which leads to a more isotropic etch. Increasing the O_2 concentration (>7.5%) results in the formation of an inorganic passivating $Si_xO_yF_z$ film on the surface. In this regime the etch rate is not longer determined by the concentration of the reactive F-ions, but is limited by the thickness of the passivation layer which needs to be etched through with ion bombardment in order to acces the Si surface [29]. In this regime the etch rate is highly dependent on the ion energy. Increasing the O_2 concentration even further (>15 %) results in dilution of the F-ion density and thus a lower etch rate. The anisotropy usually increases in the latter regime due to fast formation of the protective oxide layer but decreased side-wall attack from the F-ions [25].

As explained before, not only the pressure and the presence of O_2 determines the selectively and anisotropy of the etch. We observed that the CHF_3:SF_6 ratio turned out to be very critical as well, and can be tuned to make the etch recipe more selective for Si. However, we found that this, for all cases we tried, always results in a more anisotropic etch. The reason is that the highest selectivity can be reached if there is no protecting layer formed on the surface, increasing the Si etch rate (and thus the selectivity) and making it unnecessary to use high energy ions to remove this protective layer which also etches the SiO_x mask. Decreasing the bias generally also increases the selectivity since the etching of SiO_x is ion induced, and thus dependent on the bias. However, changing the bias will also change the Si and protective oxide layer etching, resulting in a change of anisotropy.

The optimum anisotropic etch recipe we found consists of 35 sccm CHF_3, 5 sccm SF_6, a pressure of 7 mTorr and 125 W forward power. This results in a DC-bias of about 400 V and an etch rate of $\sim$18 nm/min. Because the plasma becomes more difficult to ignite with such low pressures and no ICP power, a strike pressure of 20 mTorr was used during the first 70 s of the etching procedure. In general, we found that a lower pressure results in more anisotropic etching, but using a too low pressure results in an unstable plasma.

Figure 7 shows the results of the RIE etching process after different etching times. It can clearly be observed that the etch depth into the Si increases, while the HSQ mask is decreasing in height if the etching time increases (Figs. 7(a) and 7(b)). The disappearance of HSQ is a result of the limited selectively, which is about 1:1. Therefore the mask will be completely gone after a certain etching time (typically after 7–10 min. of etching, depending on the HSQ thickness). This is shown in Fig. 7(c). With the 200–250 nm HSQ layers as described in Section 2, we typically obtain Si coaxes of 150–200 nm in height. Etching further when the HSQ mask has disappeared results in etching of the Si rings, resulting in crown-like structures as can be seen in Fig. 7(d).

The etch is usually stopped before all the HSQ has disappeared to prevent the crown-like structures as shown in Fig. 7(d). This has the consequence that there is still a thin remaining layer of HSQ on top of the Si structures. To remove these remainders of the resist, the RIE was followed by a 1% HF dip of 10 minutes. Figure 8 shows SEM images of the structures after the HF dip. After etching, the coaxes have a wall thickness of 20–30 nm, depending on the wall thickness of the HSQ mask, as shown in Figs. 8(a) and 8(b). Figure 8(c) shows that the etch is very uniform over larger areas. Typically we etch fields of 20×20 μm.

Although the minimum wall thickness obtained with the above described procedure is about 20 nm, it can be decreased further by thermally oxidizing the samples at 950 °C for a short time (1–3 minutes) in the presence of an O_2 flow of 1 L/min. After the oxidation the oxide is removed with an HF dip. Using this method, we obtained rings of about 6 nm in thickness, as shown in Fig. 9.

#254759 Received 1 Dec 2015; revised 8 Feb 2016; accepted 8 Feb 2016; published 23 Feb 2016

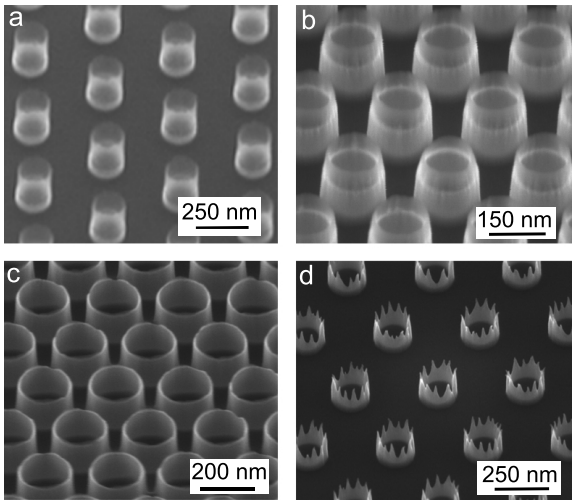

Fig. 7. RIE using SF_6 and CHF_3 after different etching times. (a) After 1 minute etching time: very short rings of Si can be distinguished underneath the HSQ mask. (b) After 5 minutes etching time: the etch depth in Si is increased, while the HSQ mask thickness is decreasing. (c) After 8 minutes etching time: the Si coaxes are 150 nm tall, there is almost no HSQ left on top of the structures. (d) After 10 minutes etching time: the Si coaxes are transformed into crown-like structures and there is no HSQ left on top of the structures. SEM images are taken using a 5 keV electron beam.

3.2. Reactive ion etching of Si using HBr

Although we obtained very smooth and anisotropic results with SF_6 and CHF_3 RIE etching, the maximum etch heights are limited due to the limited etch selectivity for HSQ. To increase the maximum etch depth in Si, we explored etch recipes using HBr, which is known to selectively and very anisotropically etch Si [31, 32]. The Si reaction rate with HBr to form the volatile $SiBr_4$ and H_2 is very small compared to other Si etchants [33], which implies that ion bombardment is necessary to obtain acceptable etch rates. The low reaction rate results in almost no side-wall etching and thus no undercutting, allowing highly anisotropic profiles to be etched without protecting the sidewalls with a passivant [34].

Because ion bombardment plays a major role in HBr etching of Si, the choice of ion flux is very important, which is not only determined by the used etched parameters, but also by the shape and material of the mask and the etched structures itself. The ion flux is dependent on the mask and etched structures since ions can scatter from the features. Furthermore, the ion flow and ion-sidewall interaction can be altered due to charging of the mask if a non-conductive mask is used. These effects can cause different results for different coax dimensions and pitches. The only way to eliminate these effects completely is to use a more radical-based etching recipe (as described in Section 3.1). However, the impact of these effects can be minimized by optimizing the etching parameters.

We found an optimized three-step recipe, where the first step is a 15 s 50 sccm Cl_2 etch at 60 °C, a pressure of 7 mTorr, 30 W FP and 750 W ICP power. This results in a bias of $\sim$110 V. This step is less selective than the HBr etch and removes the native oxide on the Si surface. The second step is a 2 minutes waiting time to pump out the Cl_2 gas. Then the actual HBr etch is started, using 48 sccm HBr, a low (2.6 mTorr) pressure and 100 W forward power. The resulting DC bias is $\sim$310 V. Images of the resulting structures can be seen in Fig. 10. The deeper areas

#254759 Received 1 Dec 2015; revised 8 Feb 2016; accepted 8 Feb 2016; published 23 Feb 2016

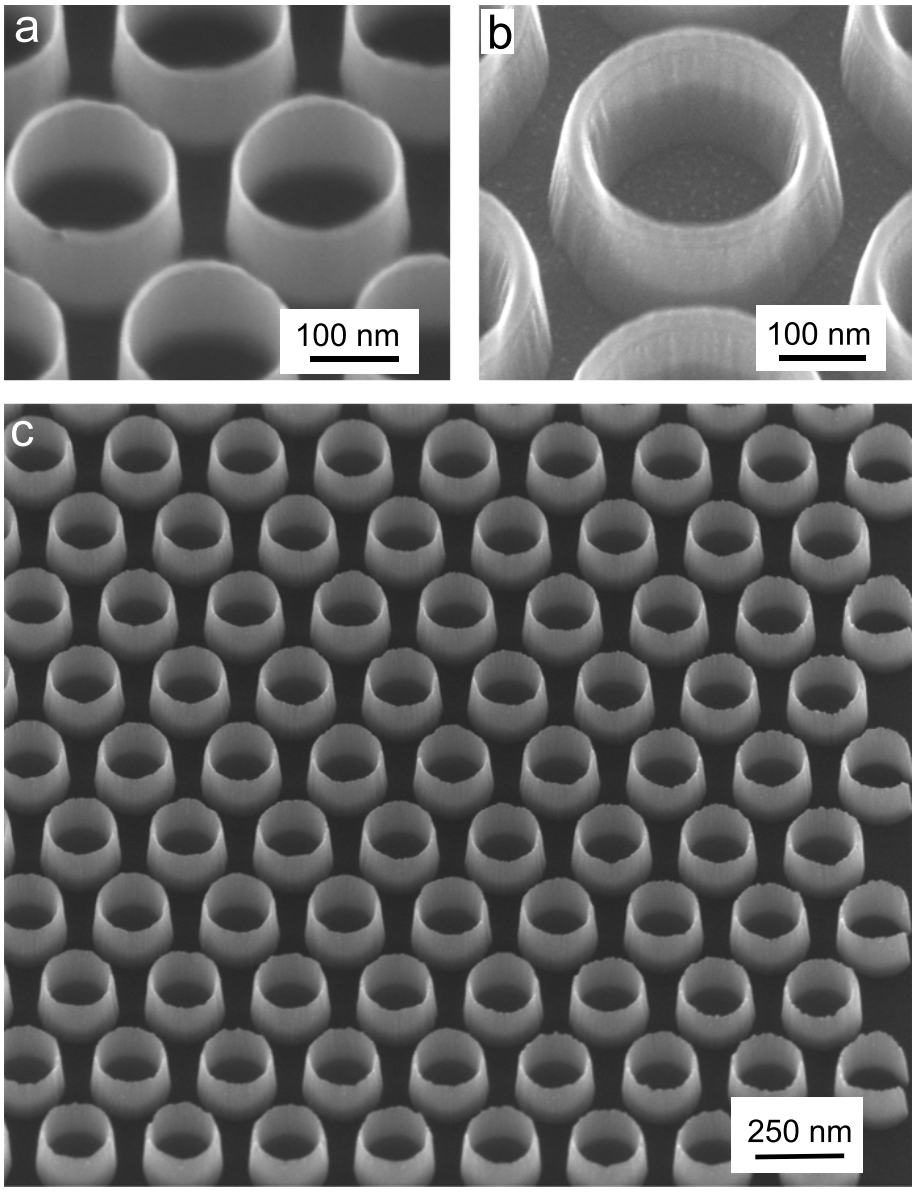

Fig. 8. SEM images of Si rings after RIE using SF_6 and CHF_3, followed by a 10 min. 1% HF dip. (a) Using an HSQ etch mask with a small and (b) a larger wall thickness. The obtained wall thicknesses after etching are 20 and 40 nm respectively. (c) The etch is uniform over the entire 20×20 μm^2 coax field. SEM images are taken using a 5 keV electron beam.

#254759 Received 1 Dec 2015; revised 8 Feb 2016; accepted 8 Feb 2016; published 23 Feb 2016

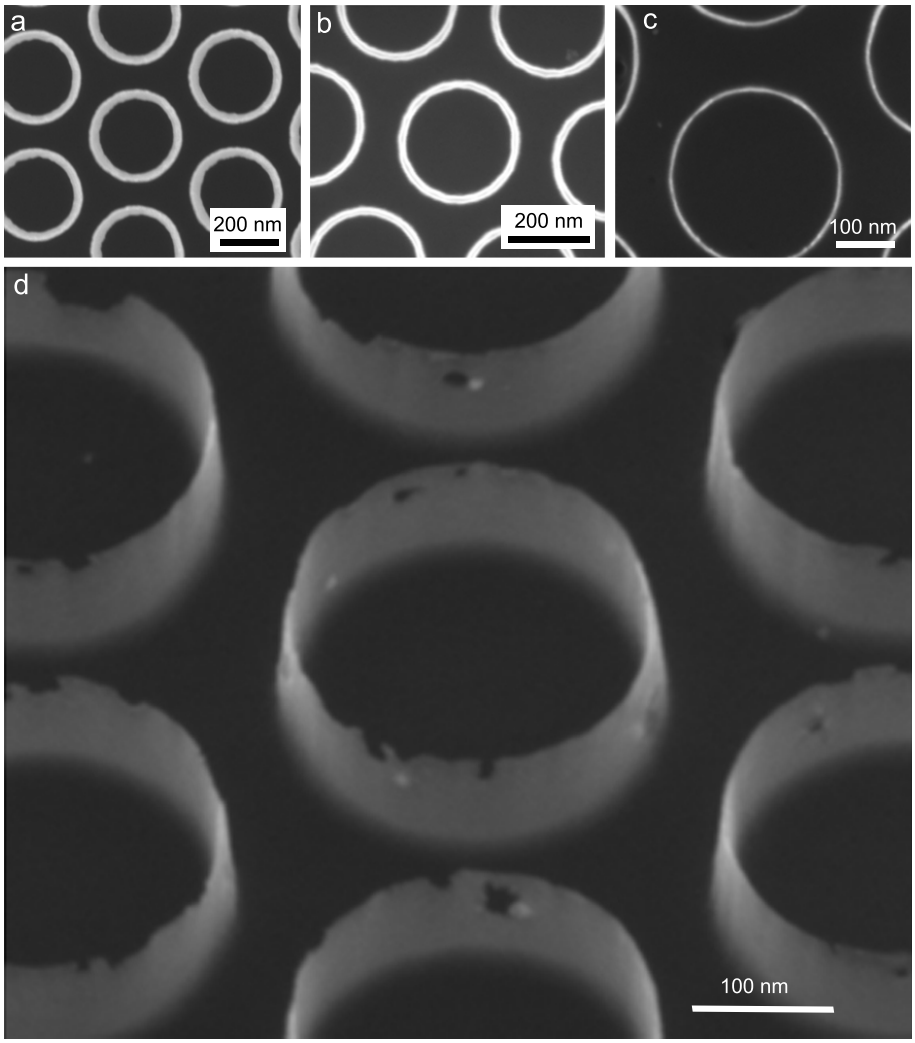

Fig. 9. Ultra-thin Si coaxes. (a) Top view SEM image of Si rings after RIE etching, having a height of 140 nm. Wall thickness is 35 nm. (b) After first oxidation, 1 minute 950 °C 1 L/min O_2 and a 5 min. 5% HF dip. The wall thickness is reduced to 15 nm. (c) Top and (d) tilted view of the Si coaxes after second oxidation for 30 s at 950 °C 1 L/min O_2 and HF (10 min. 1%) dip. The remaining wall thickness as measured with the SEM is about 6 nm. SEM images are taken using a 5 keV electron beam.

#254759 Received 1 Dec 2015; revised 8 Feb 2016; accepted 8 Feb 2016; published 23 Feb 2016

surrounding the structures in (a) are the result of ions which are scattered off the structures, hitting the substrate just next to the coaxes. We etched structures as deep as 500 nm by using a mask of 80 nm, resulting in wall thicknesses of only 10–20 nm. The HBr etch rate of Si is about 1 nm/s, while the mask etch rate is about 0.1 nm/s. However, the Cl_2 etch removes about 25 nm of HSQ in the first 15 s of the etching process, resulting in a lower overall selectivity, which is determined by the relative etch times of the two etching steps.

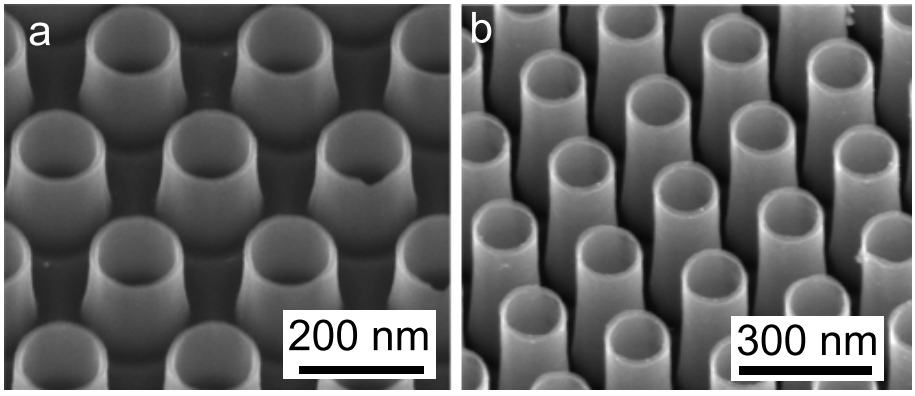

Fig. 10. SEM images of reactive ion etched Si using HBr after a 10 minutes 1% HF dip to remove the HSQ mask. (a) 250 nm tall and (b) 500 nm tall cylinders, having a wall thickness of 10–20 nm. SEM images are taken using a 5 keV electron beam.

In general, the ion impact power increases with increasing RF power and decreasing pressure. Furthermore, increasing the pressure results in a higher angular distribution of the ion flow, resulting in less anisotropy [32]. For these reasons we chose a recipe with low pressure and relatively low RF power. This agrees with our results as shown in Fig. 11, where an increase in pressure indeed leads to more isotropic etch profiles. Changing the RF power to either smaller or larger values both results in less anisotropy. This result is more difficult to predict a priori since the effect of the RF power is a balance between an enhanced etch rate by back-scattered ions upon increasing the RF power, and an increased sensitivity of the ions to charged surfaces for lower RF powers. Both effects lead to lateral etching, and thus less anisotropy.

As explained before, a sidewall passivant is not always needed using an HBr-based etch, since the etch is dominated by ion bombardment. However, especially in the case of closely packed structures, the sidewalls of the structures can be attacked by ions which are scattered off neighboring structures [34]. To protect the sidewalls from the bombardment with these off-axis ions, O_2 can be added to form a protective SiO_2 layer on the side walls [31]. However, O_2 also increases the halogen atom density by reacting with HBr to form water and Br^* radicals. These radicals can enhance lateral etching by attacking the sidewalls. We found increased isotropic etching for small O_2 concentrations, resulting in holes in the coax sidewalls as can be seen in Fig. 12. Thicker sidewalls are observed for higher O_2 concentrations, due to the formation of a protective SiO_2 layer. Increasing the O_2 concentration even more can lead to the formation of grassy surfaces, as observed in [35]. This effect is the result of micro-masking by HSQ particles which are scattered on the substrate.

Not only the anisotropy can be altered by adding O_2, the selectivity can be changed as well. O_2 binds to C-atoms which are often present as contamination in the chamber. The selectivity is altered by adding O_2 since carbon contamination leads to enhanced SiO_2 etching, by forming CO_2, which results in a less selective etch if a SiO_x containing resist is used.

#254759 Received 1 Dec 2015; revised 8 Feb 2016; accepted 8 Feb 2016; published 23 Feb 2016

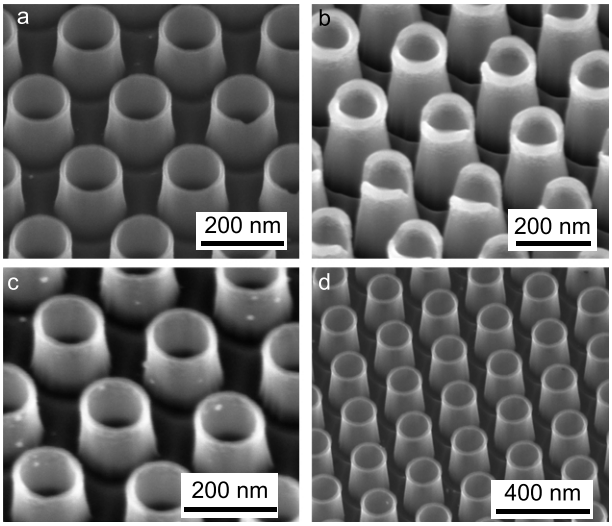

Fig. 11. Influence of changing the pressure (a,b) and the RF power (c,d) compared to the standard etch recipe for which the lowest pressure possible (2.7 mTorr) and a RF power of 100 mTorr was used. (a) P=7 mTorr, (b) P=8 mTorr. For both cases the etch was more isotropic compared to the standard etch, where the deeper etched regions surrounding the coaxes are more pronounced in the case of higher pressures. This is due to increased ion scattering from the structures. The RF power was decreased to (c) 80 W and increased (d) to 125 W. Both results in a more isotropic etch. All SEM images where taken using a 5 keV electron beam, after a 10 minutes 1% HF dip.

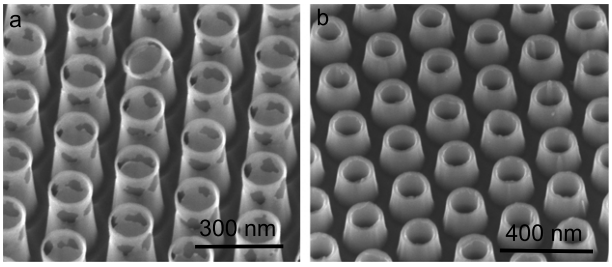

Fig. 12. The effect of adding (a) 1 sccm and (b) 10 sccm O_2 to the standard HBr etching recipe. For small O_2 concentrations the anisotropy is decreased due to increased halogen atom density, whereas for larger concentrations the sidewalls are protected with SiO_2, resulting in thicker sidewalls. The SEM images are taken after a 1% 10 minutes HF dip to remove the HSQ mask and protective oxide layer. SEM images are taken using a 5 keV electron beam.

#254759 Received 1 Dec 2015; revised 8 Feb 2016; accepted 8 Feb 2016; published 23 Feb 2016

Changing the temperature changes the relative ion/radical induced etching rates. Increasing the temperature increases the surface mobility of desorbed Br-atoms and lowers the activation energy needed for the reaction of Si with Br. Both effects change the etch rate and anisotropy. Figure 13 shows the effect of changing the temperature by 10 °C compared to the optimized recipe.

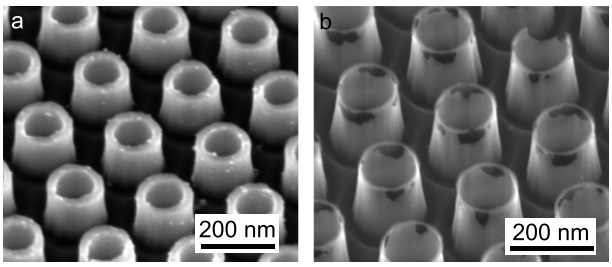

Fig. 13. The effect of (a) decreasing and (b) increasing the temperature with 10 degrees compared to the standard HBr etching recipe at 60 °C. Both SEM images show increased isotropy compared to the standard recipe. The SEM images are taken after a 1% 10 minutes HF dip to remove the HSQ mask. SEM images are taken using a 5 keV electron beam.

Lastly, we consider the influence of adding ICP power during the etching process. Generally, using ICP power results in a higher plasma density and more lateral movement of the ions. Both results in higher isotropy as can be seen in Fig. 14.

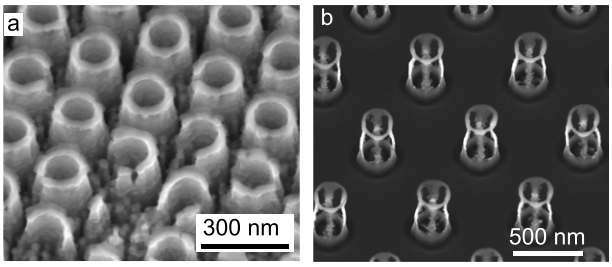

Fig. 14. SEM images of etched coaxial structures with both RF and ICP power. In (a) the standard 100 W RF power is used together with 400 W ICP power. As observed, this combination leads to micro-masking which is probably the result of HSQ sputtering in between the coaxes. In (b) the micro-masking is prevented by lowering the RF power to 30 W, in combination with an increased ICP power of 750 W. Etching with almost only ICP power results in side wall etching and thus less anisotropy. Image (a) was taken before, and (b) after an HF dip to remove the oxide. SEM images are taken using a 5 keV electron beam.

4. Metal infilling

The next step in the fabrication process is to infill the samples with metal. We demonstrate the infilling of HSQ coaxes with Ag and Au, but we successfully used the same procedure to infill Si coaxes with Ag as well.

Figures 15(a) and 15(b) shows SEM images of a sample composed of HSQ cylinders on top of a silica substrate, where the silver was thermally evaporated. The sample was aligned to

#254759 Received 1 Dec 2015; revised 8 Feb 2016; accepted 8 Feb 2016; published 23 Feb 2016

be straight above the metal crucible and a metal evaporation rate of 5 Å/s was used. As can be seen from this image, there is a metal layer growing on top of the coaxes during the evaporation. This metal mushroom shadows the near surroundings of the rings, resulting in air gaps inside the metamaterial layer. Evaporation of a thin Ge wetting layer before Ag deposition to improve the metal/dielectric adhesion does not improve the infilling sufficiently (Figs. 15(c) and 15(d)).

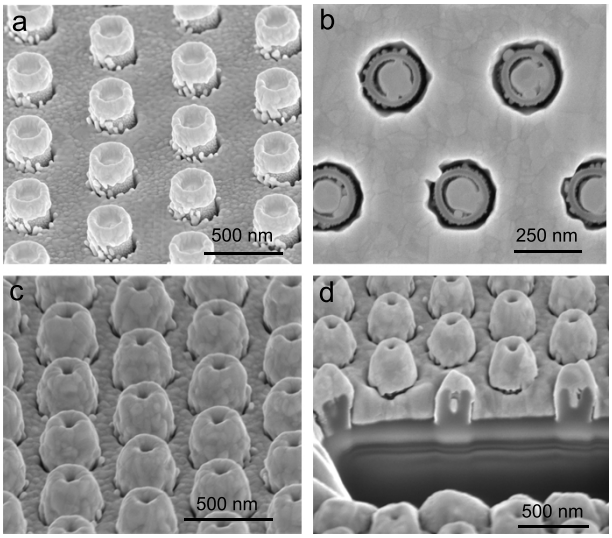

Fig. 15. Thermally evaporated silver on top of dielectric coaxial structures. (a) The Ag grows as mushrooms on top of the coaxes, shadowing the near surroundings of the rings. (b) After polishing the surface using the FIB, clear air gaps surrounding the dielectric rings are found. (c,d) A 2 nm layer of germanium was evaporated before the metal was deposited. Sample before (c) and after (d) polishing the surface with the FIB. SEM images are taken using a 5 keV electron beam.

In order to obtain fully infilled structures, we developed a new electron beam physical vapor deposition (EBPVD) method (Fig. 16). The sample is mounted at the center of a rotation stage, with the sample surface tilted slightly off-normal with respect to the silver crucible and an Ar^+ ion beam tilted 15° with respect to the sample surface. After every 15 nm of metal deposition the evaporation is stopped and a 2 mA 300 eV Ar^+ ion beam is switched on for 200 s to shave off the excess of metal growing on top of the coaxes. The sample is rotated during the entire process with 30 rpm. To reduce the grain size, which gives better infilling, but slightly worse optical properties of the metal, we used relatively high evaporation rates of 1–5 Å/s.

Figure 17 demonstrates the effect of the new method. Clearly, a significant reduction of air gaps surrounding the coaxes is observed using this new technique compared to Fig. 15. The better infilling is due to minimization of shadowing effects from metal deposited on top of the semiconductor cylinders during the metal deposition. There is still some excess of metal on top of the structures. This could be avoided by further tuning of the evaporation:milling rates.

Although this evaporation method works well, it is not straightforward to align the sample correctly with respect to the metal vapor and the argon beam. Figure 18 shows SEM images of samples which were aligned differently during the metal infilling process. The infilling is optimal if the metal vapor is slightly tilted off-normal with respect to the sample surface. This means that it is important to rotate the sample during evaporation as otherwise the resulting samples show asymmetric infilling, as can be seen in Figs. 18(a) and 18(b). Figures 18(c) and 18(d)

#254759 Received 1 Dec 2015; revised 8 Feb 2016; accepted 8 Feb 2016; published 23 Feb 2016

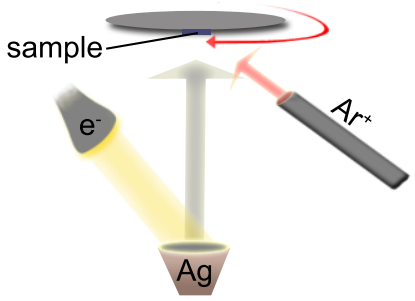

Fig. 16. Sketch of the EBPVD setup used for the metal infilling: the sample is mounted on a rotation stage above the metal crucible, with the sample surface a few degrees off-normal with respect to the metal crucible. An argon ion gun is mounted with an angle of 15° with respect to the sample surface.

shows the result if the sample surface was normal to the metal vapor. In between the rings (for larger pitches), the structures are nicely infilled. However, an air ring is seen between the coax center and the inner side of the dielectric ring. This can be explained by considering the non-polished image, where can be seen that the metal grows on top of the rings and thereby shadows the core.

In Figs. 18(e) and 18(f) the sample was tilted to the other direction, such that the angle between the sample surface and the metal crucible was increased. In this configuration the coaxes shadow each other, resulting in metal accumulations in between the coaxes, at the positions where the shadowing is minimal. The infilling of the center of the coaxes show the opposite behavior as in Figs. 18(c) and 18(d). In this case the rings are completely covered with metal, but an air gap appears in the center of the rings on the bottom of the coaxes. This is the result of the oblique evaporation, the metal deposits on the cylinder walls, thereby covering and closing the gap. In this case careful investigation of the result is required, because after a shallow polish of the cylinder the infilling seems to be very conformal. However, if the polishing is continued an air gap underneath the completely infilled center is revealed. Figure 18(g) shows the effect of changing the angle of the argon ion gun with respect to the metal vapor. Lastly, Fig. 18(h) shows that there is an upper limit on the evaporation rate. Evaporating too fast results in metal sputtering, where large spheres of metal are deposited all over the sample surface.

As explained above, the alignment of the sample with respect to the ion beam and metal crucible is crucial in order to get metal infilling without any air voids. It is essential to slightly tilt the sample surface with respect to the metal crucible, which limits the maximum aspect ratio of the coaxes that we can infill. A SEM image of a high aspect ratio coax is shown in Fig. 19(a). We found similar trends as in Fig. 18(c,d); the side walls are completely covered with metal, but air gaps are found inside the center of the cylinders due to the excess metal on top of the coaxes which close the gap. In order to investigate this in a more controlled way, the metal infilling of cylinders with slightly different aspect ratios is considered (Figs. 19(b)- 19(d)). In case of the smallest aspect ratio (largest ring diameter), both the walls are covered with metal and the center areas are infilled. Increasing the aspect ratio results in air gaps underneath filled coaxes, whereas decreasing the ring diameter further results in filled coaxes again. In case of the latter, the coaxes are too small in order to evaporate metal on the inner side walls of the cylinders. However, due to the rotation of the sample during the evaporation process, there is metal deposition in the center of the coax. Due to the small inner diameter, the metal in the

#254759 Received 1 Dec 2015; revised 8 Feb 2016; accepted 8 Feb 2016; published 23 Feb 2016

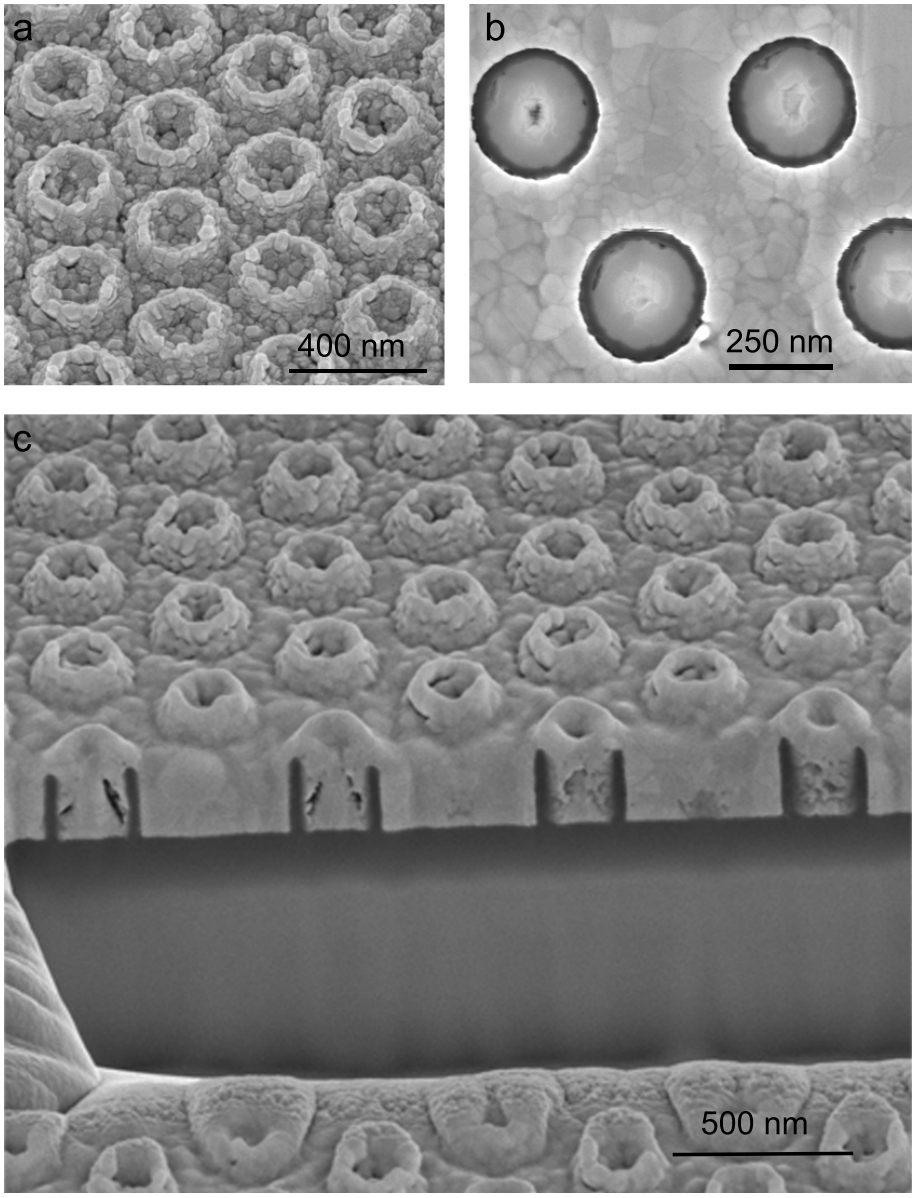

Fig. 17. Results of the newly developed EBPVD method. SEM images of dielectric coaxes embedded in metal before (a) and after (b) polishing the surface with the FIB. (c) Cross section of the same sample shown in (a). These samples show a significant reduction of air voids compared to the SEM images shown in Fig. 15. SEM images are taken using a 5 keV electron beam

#254759 Received 1 Dec 2015; revised 8 Feb 2016; accepted 8 Feb 2016; published 23 Feb 2016

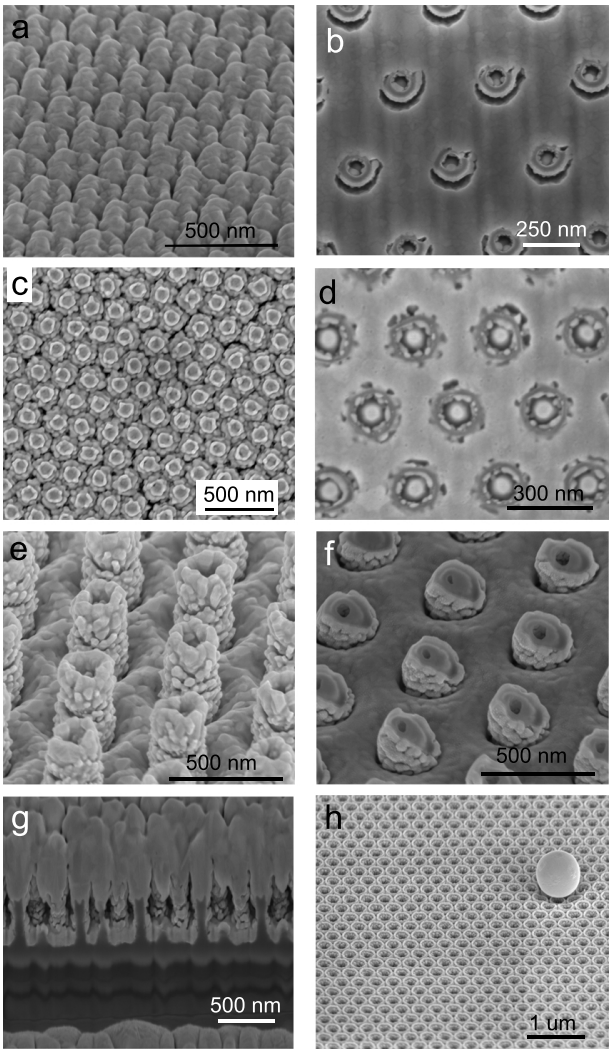

Fig. 18. Alignment issues during the metal infilling process. (a,c,e,g,h) Are taken before and (b,d,f) after polishing with the FIB. (a,b) The gold infilling is performed without rotating the sample during the evaporation process. (c,d) The sample was rotated during the infilling process, with the sample surface tilted normal with respect to the gold crucible. (e,f) The sample as rotated, but tilted too far with respect to the metal crucible, such that the angle between the sample surface and the metal vapor was larger then in the optimal case. (g) Ion gun was mounted under 45° instead of 15° with respect to the sample surface. (h) The evaporation rate was too high (>5 Å/s), resulting in large metal spheres which are sputtered over the sample surface. SEM images are taken using a 5 keV electron beam.

#254759 Received 1 Dec 2015; revised 8 Feb 2016; accepted 8 Feb 2016; published 23 Feb 2016

center does reach the inner walls, resulting in full infilling of the sample. The latter process only works successfully in case of shallow coaxes, since the center of the coax will be shadowed after a while by the excess of metal growing on top of the coaxes.

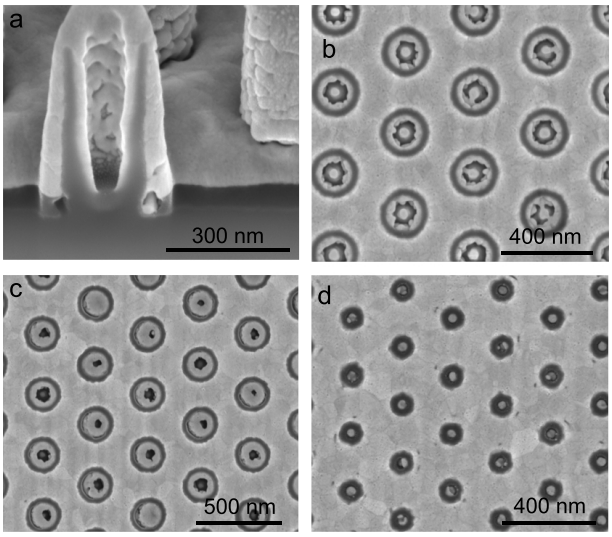

Fig. 19. Sample limitations for the metal infilling process. (a) Cross section of a 350 nm tall coax having a diameter of 180 nm. The ring itself is covered with gold, but the inner core is completely empty. (b-d) 260 nm tall coaxes with a diameter of 200, 150 and 100 nm respectively. Images of (b-d) taken after polishing the surface with the FIB. SEM images are taken using a 5 keV electron beam.

5. FIB polishing

Although we do mill the excess of metal growing on top of the coaxes during the metal deposition process, the sample surface is still fully covered with metal after the deposition, as discussed in Section 4. To smoothen the surface and make the samples optically accessible we use the gallium ion beam of the FIB as shown in Fig. 20(a): we come in with the ion beam under very grazing angles (4–5° with respect to the sample surface) and ideally only mill the excess of metal. For the Si membrane samples, determination of the exact angle with respect to the ion beam is difficult, due to the bending of the stressed silicon which varies with position on the sample.

To align, we tilted the stub to the point where the sample surface could just be seen with the ion beam and the square coax arrays (20×20 μm^2 typically) appear as thin lines (the side walls of the fields). Then, a rectangular box was drawn of typically $x = 20$ μm^2 (which was usually the length of the coax field), $y = 200$ nm. Here, we defined x as the horizontal axis, along the base of the coax field, and y will now define how much the beam will scan in height over the sample. The voltage was 30 kV, and typically we used a current of 48 pA. In this way, we succeeded in making smooth surfaces of about 20×20 μm^2 within several minutes. SEM images of the resulting samples can be seen in Fig. 21. Figure 20(b) shows a SEM image halfway during the shaving process: the top half of the coax field is exposed, whereas the lower half in the image is still fully covered with metal.

For this procedure the right alignment of the sample with respect to the ion beam is crucial. Firstly, we consider the shaving angle. If the angle is too steep, the resulting fields show a large

#254759 Received 1 Dec 2015; revised 8 Feb 2016; accepted 8 Feb 2016; published 23 Feb 2016

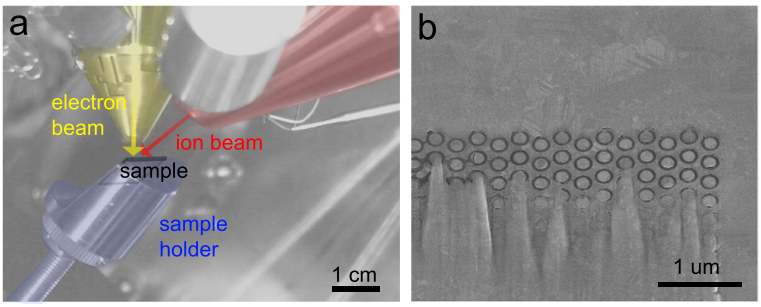

Fig. 20. FIB polishing process. (a) Sketch of the setup inside the SEM: a special stub was used to be able to mount the sample such that is is tilted with respect to the ion beam such that the ions come in under an angle of a few degrees. (b) Top view SEM image halfway the polishing process: the dark rings are the Si coaxes which are revealed as the silver is milled away. SEM images are taken using a 5 keV electron beam.

gradient in thickness, as can be seen in Fig. 22(a). The dark grey area on the top of the SEM image is Si, meaning that all the silver is removed, while on the bottom side there is almost no Si visible, meaning that we did not polish deep enough. In order to get the gradient as small as possible, we need to tilt the sample to more grazing incidence angles. However, if the angle is too small, we find sharp grooves in between the coaxes (see Fig. 22(a)). These grooves are the result of shadowing effects. Coaxes in the path of the ion beam shadow the coaxes in front of them. As expected, this effect becomes more pronounced the further away we polish from the first row in the field, which can be seen in Fig. 22(b). Also other objects in the ion path can give this problems, like dust or sputtered metal in front of the coax fields.

The *y*-size of the box is an important parameter to consider. If it is too small only a small stroke is polished, if it is too big we find again the pronounced grooves due to shadowing of other parts of the sample. The *y*-value defines the height of the ion beam compared to the sample surface, if the range for this value is too big, we start scanning at low positions of the ion beam, meaning that the beam is not grazing over the surface, but hits the side wall of the field. The rings are more resistant to the ion beam than the metal in between, resulting in grooves in between the rings, as can be seen in Fig. 22(c).

Milling under normal incidence results in a very rough surface and doesl not selectively etch the excessive metal. Figure 22(d) shows a SEM image of a field which was very shortly exposed to the ion beam under normal incidence. The metal immediately deforms, resulting in very rough surfaces.

6. RIE backside etch

Finally, in case of the Si membrane samples, we perform a backside etch to thin the substrate, using the same etch recipe as for etching the silicon coaxes into the silicon substrate. Figures 23(a) and 23(b) shows the result if the etch was too long. As can been seen in Fig. 23(c), the metamaterial was not made completely free-standing, since the etch rate, and therefore the Si thickness, varies over the sample due to the bending of the membrane. Furthermore, we cannot measure the thickness while etching, making it very difficult to stop precisely at the back-surface of the metamaterial; all Si is etched away and only the metal remained. The coaxes have fallen out of the metal template. Typically 50–100 nm of the Si membrane remains to support the metamaterial.

The final metamaterial, as shown in Figs. 21 and 23(c), do show some fabrication imper-

#254759 Received 1 Dec 2015; revised 8 Feb 2016; accepted 8 Feb 2016; published 23 Feb 2016

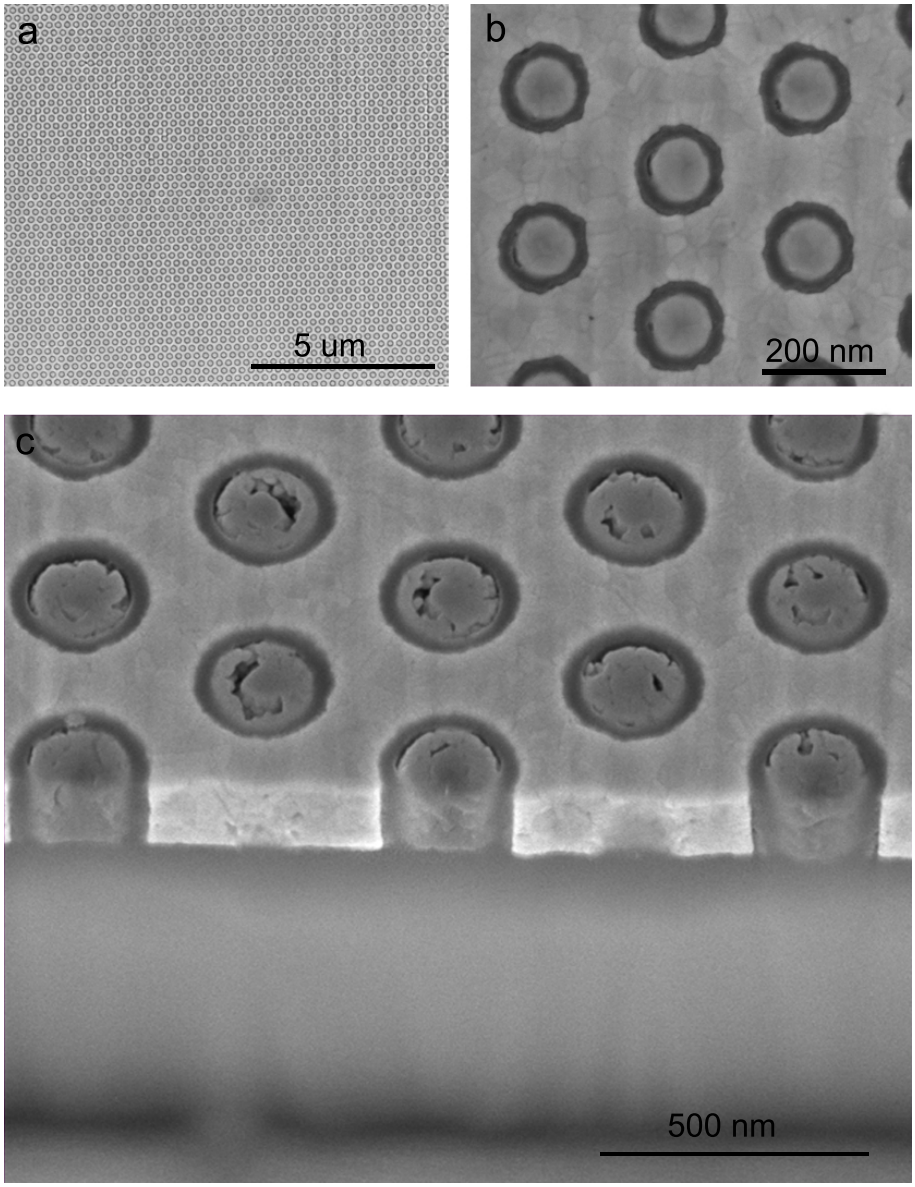

Fig. 21. SEM images of the final metamaterial sample: the dielectric coaxes appear as dark lines embedded in the lighter colored metal. (a) Top view of a 15×15 μm^2 area, (b) top view of a small area and (c) cross section. SEM images are taken using a 5 keV electron beam.

#254759 Received 1 Dec 2015; revised 8 Feb 2016; accepted 8 Feb 2016; published 23 Feb 2016

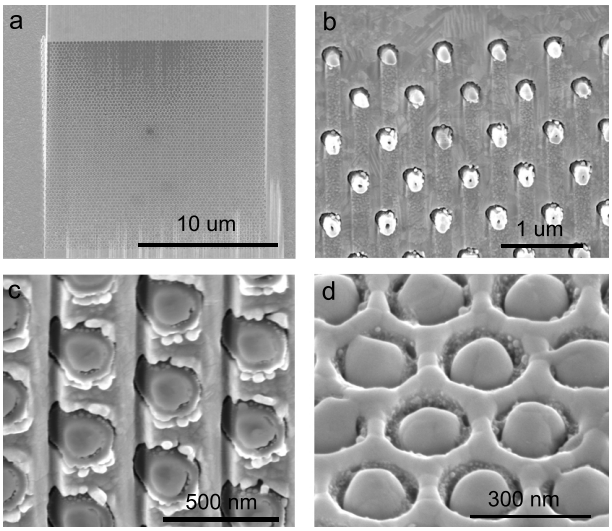

Fig. 22. FIB polishing alignment problems. (a) Top view of a $20 \times 20\ \mu m^2$ coax field after FIB polishing. The dark area on the top side is bare Si, where all coaxes have been shaven away. On the bottom fully metal covered coaxes are observed. (b,c) Shadowing of the coaxes: pronounced grooves appear during the polishing process. The ions come in from the top side. (d) Very short (<2 s) exposure of the ion beam under normal incidence. SEM images are taken using a 5 keV electron beam.

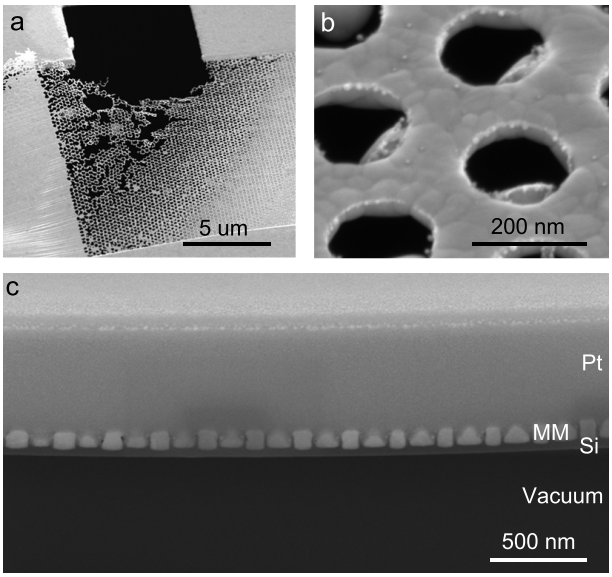

Fig. 23. Back side etching of the Si membrane samples. (a,b) The Si was etched for too long, only the metal remained. The black square on (a) is a reference hole for the measurements. (c) Cross section of a finished 91 nm thick metamaterial sample on a Si membrane of only 17 nm. Pt was deposited to make a better cross section. SEM images are taken using a 5 keV electron beam.

#254759 Received 1 Dec 2015; revised 8 Feb 2016; accepted 8 Feb 2016; published 23 Feb 2016

fections like slightly conical shaped rings or imperfect metal infilling. These imperfections will have an influence on the optical properties. However, very good agreement of the simulated/calculated optical properties, where the rings are assumed to be perfectly straight, and the experiments on the fabricated coaxes have been found [12]. From these experimental results we conclude that the fabrication imperfections only have small effects on the optical properties.

7. Conclusions

In conclusion, we have described the fabrication process of a coaxial plasmonic metamaterial using a combination of electron beam lithography, reactive ion etching, electron beam physical vapor deposition and focused ion beam milling. Using this process we successfully fabricated the metamaterial both on glass and silicon and infilled the waveguides with either silver or gold. Freestanding structures were fabricated starting with a 1 μm thick silicon membrane.

Acknowledgments

We would like to thank Hinke Schokker for her efforts on developing the fabrication process and Anja van Langen-Suurling from TU Delft for her help and support on the 100 keV EBL process. This work is part of the research program of the Stichting voor Fundamenteel Onderzoek der Materie (FOM), which is financially supported by the Nederlandse Organisatie voor Wetenschappelijk Onderzoek (NWO). It was also funded by NanoNextNL, a technology program of the Netherlands Ministry of Economic Affairs and the European Research Counsel.

#254759 Received 1 Dec 2015; revised 8 Feb 2016; accepted 8 Feb 2016; published 23 Feb 2016